Robust 3D Point Cloud Registration Exploiting Unique LiDAR Scanning Pattern

Ahmad Kamal Aijazi[a] and Paul Checchin[b]

Institut Pascal, UMR 6602 CNRS Université Clermont Auvergne, F-63000 Clermont-Ferrand, France

Keywords: LiDAR, Non-Repetitive Scanning, 3D Point Cloud and Scan Registration.

Abstract: The task of 3D point cloud registration is fundamentally about aligning multiple scans or point clouds obtained from one or more LiDAR sensors to create a unified and accurate representation of the scanned scene. This process serves as the cornerstone for applications such as map building, autonomous navigation, land surveying and many others. While 3D registration techniques have made significant advancements, several persistent challenges continue to warrant research attention and innovation. Recently, non-repetitive scanning LiDAR sensors are emerging as a promising alternative for 3D data acquisition. In this paper, a novel 3D point cloud registration method is presented that exploits the unique scanning pattern of the sensor to register successive 3D scans. The sensor is first characterized and then, using the characteristic equation of the unique scanning pattern, a perfect scan is reconstructed at the target distance. The real scan is then compared with this reconstructed scan to extract objects in the scene. The displacements of these extracted objects in successive scans, with respect to the center of the unique scanning pattern, are compared in successive scans to determine the transformations that are then used to register the successive scans. The proposed method is evaluated on two real and different datasets and compared with other state-of-the-art registration methods. The results show that the method is comparable with other methods in terms of accuracy but surpasses them in performance in terms of processing time.

1 INTRODUCTION

The advancement of LiDAR (Light Detection and Ranging) technology has played a pivotal role in revolutionizing our ability to capture three-dimensional representations of the environment with unprecedented accuracies and details. The task of 3D point cloud registration is fundamentally about aligning multiple scans or point clouds obtained from one or more of these LiDAR sensors to create a unified and accurate representation of the scanned scene. However, the process of registering multiple LiDAR-generated point clouds into a single, coherent 3D model is not without its challenges.

Most of the state-of-the-art methods employ repetitive scanning LiDAR sensors which have their inherent limitations. Recently, non-repetitive scanning LiDAR sensors are emerging as a promising alternative for 3D data acquisition. In this paper, we explore the use of such a LiDAR sensor to improve the 3D point cloud registration process using its unique scanning pattern.

2 RELATED WORK

Point cloud registration is an important task for localization and mapping applications. In this section, we review some key research in the field of 3D point cloud registration.

The Iterative Closest Point algorithm (ICP) proposed by Besl and McKay (1992) has been an elementary method in point cloud registration. In this method, the distance between corresponding points in two point clouds is iteratively minimized, allowing for rigid transformation estimation. Extensions, such as the Generalized ICP (GICP) by Segal et al. (2009), dense normal based ICP (NICP) (Serafin and Grisetti, 2015) and Sample Consensus ICP (Xie et al., 2022) have improved robustness to various scenarios.

Tazir et al. (2018) modified the method for selecting 3D points for the matching process in the standard ICP algorithm to propose Cluster Iterative Closest

[a] https://orcid.org/0009-0000-6349-128X
[b] https://orcid.org/0000-0002-2930-3393

Aijazi, A. and Checchin, P.
Robust 3D Point Cloud Registration Exploiting Unique LiDAR Scanning Pattern.
DOI: 10.5220/0012342600003654

In *Proceedings of the 13th International Conference on Pattern Recognition Applications and Methods (ICPRAM 2024)*, pages 679-686
ISBN: 978-989-758-684-2; ISSN: 2184-4313

Point (CICP) that successfully register point clouds of different densities obtained form different sensors. Another variant Global ICP (G-ICP) presented by Aijazi et al. (2019) employs bundle adjustment to fine tune the registration process, at the end, in addition to the scan by scan registration using point to plane matching. However, such method is not suitable for real-time processing.

Feature-based registration methods focus on extracting distinctive features from point clouds and matching them to establish correspondences. The SIFT-based approach by Rusu et al. (2009) and the Fast Point Feature Histograms (FPFH) by Rusu and Cousins (2011) are notable examples.

One of the important concerns for point cloud registration is scalability. The LeGO-LOAM system by Xue et al. (2022) offers a real-time solution for large-scale point cloud registration and mapping. Recent advances in deep learning have led to the emergence of deep neural networks for point cloud registration (Pais et al., 2019; Choy et al., 2020).

Some works have also employed recently developed non-repetitive scanning LiDARs. The work has also been done to register their point clouds. An extension of classical feature-based methods, the work by Wang et al. (2021) introduced a feature-based registration algorithm employing point clouds generated by non-repetitive scanning LiDARs leveraging distinct features to establish correspondences. Wang et al. (2023) proposed a novel method that leverages deep learning techniques for sparse point cloud registration, achieving impressive results in various scenarios. He et al. (2021) introduced a highly efficient algorithm designed for non-repetitive scanning LiDARs, combining geometric and learning-based approaches to improve speed and accuracy. Li et al. (2023) presented a registration method for combining non-repetitive scanning LiDAR point clouds with RGB-D data, enabling precise 3D scene reconstruction. Zou et al. (2023) presented a plane-based global registration (PGR) approach for coarse registration followed by an ICP algorithm to register point clouds.

In this paper, we present a fast 3D scan registration method exploiting the unique scanning pattern of a LiDAR sensor. To the best of our knowledge, no work has so far exploited the non-repetitive scanning pattern to register point clouds.

In the following sections, we first explain the LiDAR sensor and its characterization (Section 3) and then our method (Section 4). The experiments and results are presented in Section 5 while we conclude in Section 6.

3 CHARACTERIZATION OF NON-REPETITIVE SCANNING LIDAR

The recently developed Mid-70 sensor by LIVOX is a solid state 3D LiDAR. The sensor is capable of collecting up to 100 000 points per second within a circular field of view directly in front of the scanner's glass window. With a small form factor, it has a range of about 260 m with precision of up to 0.02 m (see Table 1 for more specifications). However, what really sets this sensor apart from other laser scanners is its scanning mechanism. Rather than rotate the laser scanner/receiver pair themselves (as is done in a multi-line scanner like Velodyne LiDARs), this holds the two in a "solid state", immobilized inside the scanner's housing while the outbound and inbound light is directed through a pair of Risley prisms (Brazeal et al., 2021). These wedge-shaped glass lenses act as optical steering mechanisms as they rotate in opposite directions, directing the beam in a rosette-style scan pattern in the circular scan area (Figure 1).

Table 1: Main specifications of the used sensor.

Main specifications	
Laser Wavelength	905 nm
Detection Range	260 m @ 80% reflectivity
Field of view	70° circular
Range Precision	0.02 m
Beam divergence	0.28° (vert.) × 0.03° (horiz.)
Dimension	97 × 64 × 62.7 mm

A rosette is a set of points in polar coordinates (r, θ) specified by the polar equation:

$$r = a\cos(k\theta) \tag{1}$$

or in Cartesian coordinates (x, y) using the parametric equations:

$$x = r\cos(\theta) = a\cos(k\theta)\cos(\theta) \tag{2}$$

$$y = r\sin(\theta) = a\cos(k\theta)\sin(\theta) \tag{3}$$

where a is the amplitude or size factor, k the angular frequency. The rose specified by $r = a\sin(k\theta)$ is identical to that specified by $r = a\cos(k\theta)$ rotated counter-clockwise by $\frac{\pi}{2K}$ radians, which is one-quarter the period of either sinusoid. If k is odd, the rosette is k petaled. If k is even, the rosette is $2k$ petaled.

In order to exploit the scanning pattern of the LiDAR sensor, we need to characterize its scanning pattern by determining the value of a and k. To determine these parameters, we positioned the sensor on a tripod stand in front of a plane surface as shown in Figure 2.

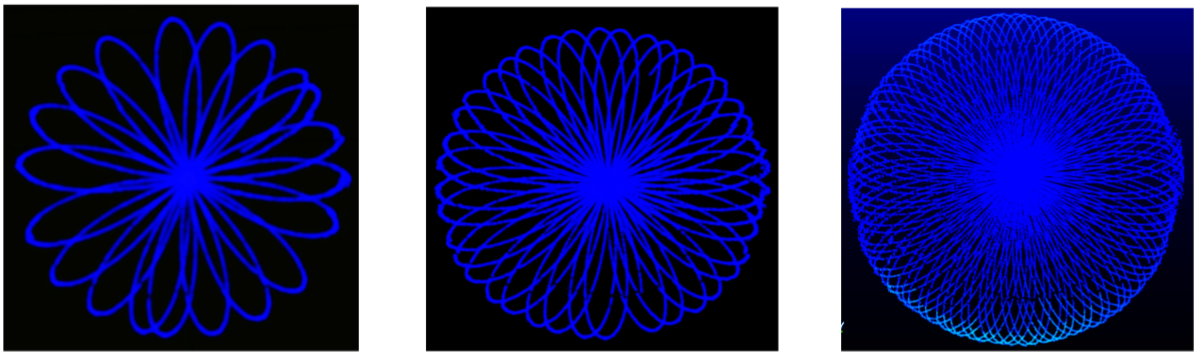

(a) 100 ms (b) 200 ms (c) 400 ms

Figure 1: Rosette – style scanning pattern of the sensor scans at different integration time.

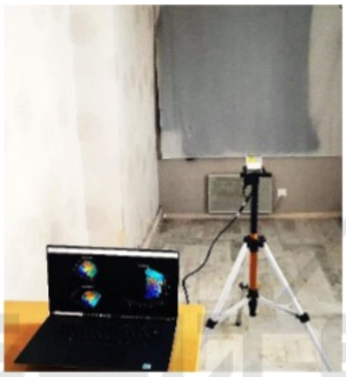

Figure 2: Experimental setup.

In order to determine the value of k, the different scans obtained from the sensor were analyzed (the form and number of petals) at different integration times, as shown in Figure 1. The number of petals found was 200 per second. Being an even number, this equates to a value of $k = 100$.

We considered the value of a as a function of scanning distance. The distance of sensor was varied from 1 to 50m at regular intervals and the successive scan patterns obtained were studied. Figure 3 presents the size (in terms of diameter) of the rosette scan in terms of distance.

Using a linear approximation, the value of a was found to be:

$$a = 1.4 \times d \tag{4}$$

where d is the target distance.

4 3D SCAN REGISTRATION

The scans are registered one by one in succession. In order to register two successive scans s^{o}_{i} and s^{o}_{j}, where i and j are the number of scans, we first reconstruct each scan (Rosette-style) at the specified target

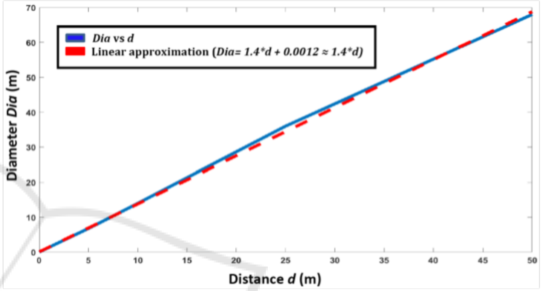

Figure 3: The size (in terms of diameter) of the rosette scan with respect to the target distance.

distance d applying the equations (2) and (3) using the values of k and a determined in the previous section. The distance d in (4) is taken as the distance of the farthest vertical plane, perpendicular to the sensor plane, detected in each scan.

The centres c^{r}_{i} and c^{r}_{j} of the successive reconstructed Rosette-style scans s^{r}_{i} and s^{r}_{j} are first aligned and then in the second step their orientations are aligned and rotations around the three axes, i.e. θ_x, θ_y and θ_z respectively, are estimated as shown in Figure 4.

In order to align the orientation, the surface normal vector is estimated for each of the reconstructed scan using Principal Component Analysis (PCA) (Klasing et al., 2009). Given a set of points in each reconstructed scan $D = x_{i(i=1)}^{np}$, the PCA surface normal approximation for a given data point $p \in D$ is typically computed by first determining the K-Nearest Neighbors, $x_K \in D$, of p. Given the K neighbors, the approximate surface normal is then the eigenvector associated with the smallest eigenvalue of the symmetric positive semi-definite matrix:

$$V = \sum_{k=1}^{K} (x_k - \overline{p})^T (x_k - \overline{p}) \tag{5}$$

where $\overline{p}$ corresponds to the centers c^{r}_{i} and c^{r}_{j} of the

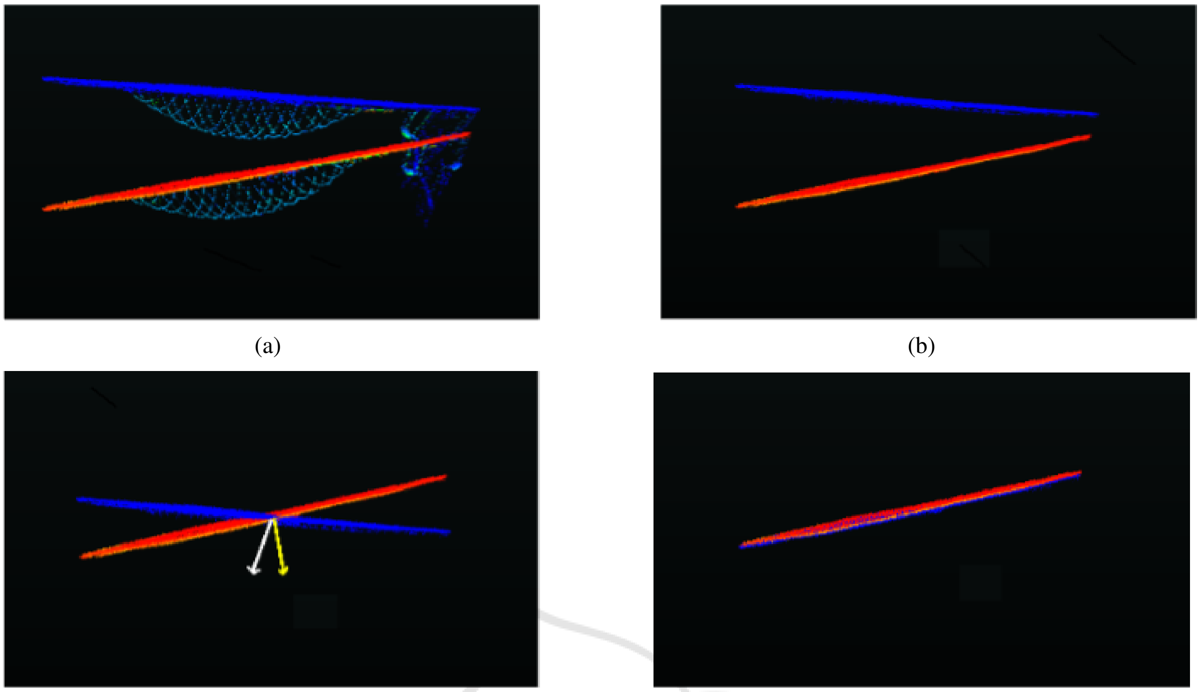

(a)

(b)

(c)

(d)

Figure 4: Figure (a) shows the two original successive scans with objects. Figure (b) presents the reconstructed scans corresponding to the two original scans without objects. In (c), the centers of the two scans are aligned, and normal vectors estimated while in (d) the second scan is rotated to align with the first scan and the difference of normal vectors give $\theta_x, \theta_y, \theta_z$.

successive reconstructed Rosette-style scans s^r_i and s^r_j.

The rotation around the three axis is then estimated as the difference between the orientation of the two normal vectors. As the sensor remains on the ground, the rotation in successive scans around the axe perpendicular to the sensor plane is considered zero.

$$\begin{aligned} \theta_x &= (\theta_{x1} - \theta_{x2}) \\ \theta_y &= (\theta_{y1} - \theta_{y2}) \\ \theta_z &= (\theta_{z1} - \theta_{z2}) \approx 0 \end{aligned} \tag{6}$$

where θ_{x1}, θ_{y1}, θ_{z1} and θ_{x2}, θ_{y2}, θ_{z2} are the orientations of the two vectors with respect to x, y and z axis, respectively.

The original scans s^o_i and s^o_j are then matched with the corresponding reconstructed scans s^r_i and s^r_j. As the reconstructed scans are free of objects, this allows the extraction of objects present in the original scans leaving behind holes. The reconstructed scans help complete the farthest and largest vertical plane in the original scans occluded by objects in the scene. All 3D points lying outside this vertical plane are then considered as object points and are extracted out leaving behind holes. The centroid P of the resulting holes in the original scans are calculated using a bounding box around each hole (or extracted object) with respect to c^o_i and c^o_j as shown in Figure 5. The displacement of these centroids with respect to the centre of the scans in the successive scans provides us with the translation, i.e. $t_{x,y}$, between the two successive scans:

$$t_{x,y} = \frac{1}{n}\sum_{m=1}^{n}\left((P^m_j - c^o_j) - (P^m_i - c^o_i)\right) \tag{7}$$

where n is the total number of holes (due to extracted objects) in the scans, P^m_i and P^m_j are the centroids of the m^{th} hole in the scans s^o_i and s^o_j, respectively. The displacement along the z axis is denoted $t_z = (d_i - d_j)$, where d_i and d_j are the distances of the farthest vertical plane, perpendicular to the sensor plane, detected in each scan, respectively.

These rotations $\mathbf{R}(\theta_x, \theta_y, \theta_z)$ and translations $\mathbf{T}(t_x, t_y, t_z)$ are then used to transform the original scans, with the first scan taken as reference, using (8). The transformed scan and the reference scan are then aggregated (9) to form the new reference scan for the next scan.

$$\hat{s}^o_j = \mathbf{R}.s^o_j + \mathbf{T} \tag{8}$$

$$s^o_{i+1} = \hat{s}^o_j + s^o_i \tag{9}$$

The method is summarized in Algorithm 1.

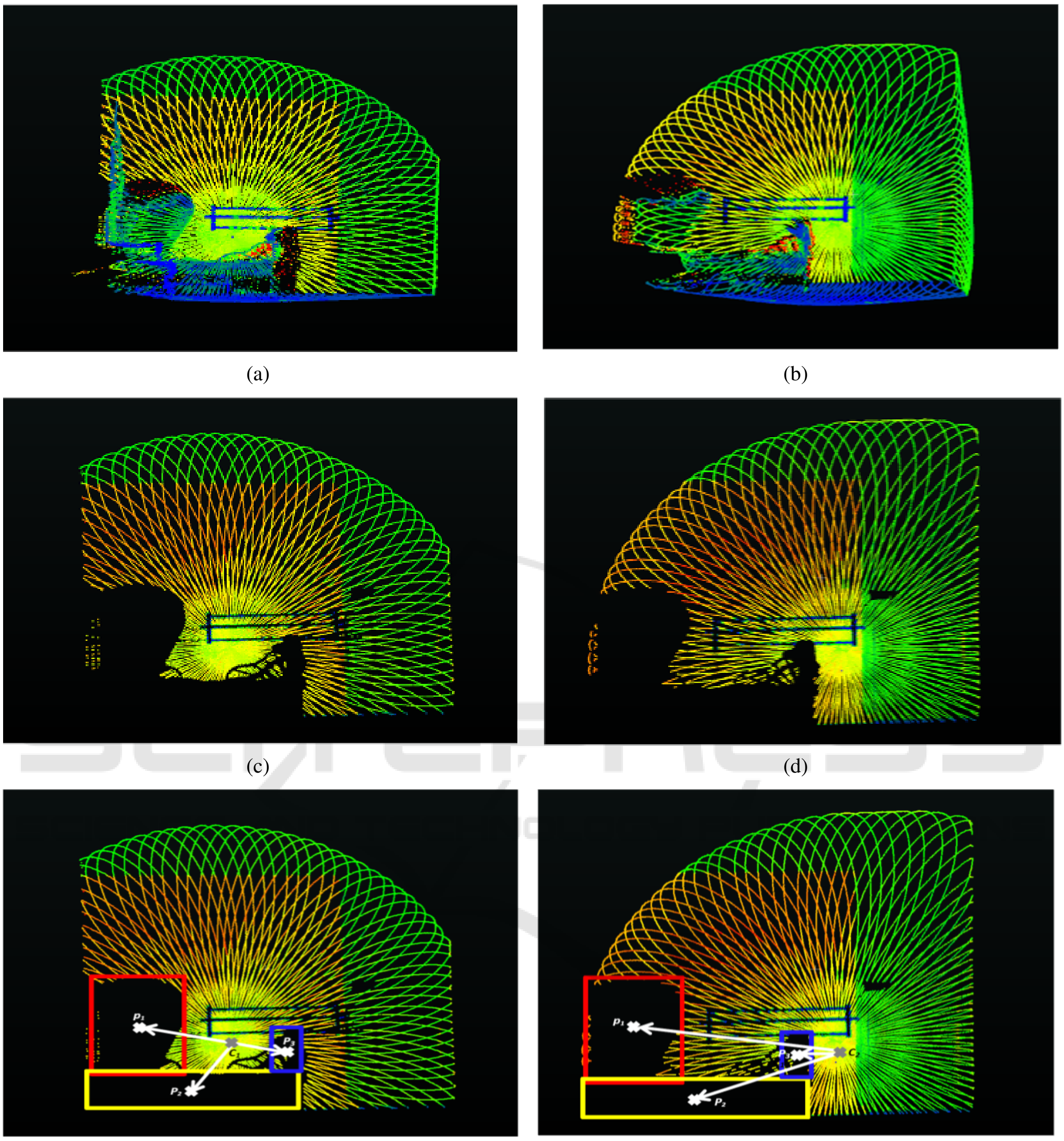

(a) (b) (c) (d) (e) (f)

Figure 5: Figures (a) and (b) show the two original successive scans with objects. (c) and (d) present the two scans with holes after extraction of objects. (e) and (f) show the bounding box around the different holes in both scans, along with their centroids and the vectors from the center of the scans and the centroids. The difference in these vectors (displacement of objects with respect to the scan center) provides us the estimates of t_x and t_y.

5 EXPERIMENTS AND RESULTS

In order to evaluate the proposed method, the sensor was employed in two different modes. In the first mode, it was mounted on a tripod and moved around different positions to completely scan an indoor room equipped with furniture (Experiment 1) while in the second mode, it was mounted on a small mobile robot moving on a predefined trajectory, at a speed of about 1 $\mathrm{m\,s^{-1}}$, scanning an enclosed hangar/parking

```
Data: 3D scans $s^{o}_{i}$ and $s^{o}_{i+1}$
Result: $s^{o}_{i+1} = \hat{s}^{o}_{i+1} + s^{o}_{i}$
for $i \leftarrow 1$ to total number of scans do
    Reconstruct Rosette style scan $s^{r}_{i}$ and
      $s^{r}_{i+1}$ at distance of farthest vertical plane
      detected;
    Align centers of $s^{r}_{i}$ and $s^{r}_{i+1}$;
    Estimate the surface normal vector $V$ for
      $s^{r}_{i}$ and $s^{r}_{i+1}$;
    Estimate the rotations $\theta_x$, $\theta_y$, $\theta_z$ as
      difference of orientation between the
      two normal vectors;
    Compare $s^{o}_{i}$ and $s^{o}_{i+1}$ with $s^{r}_{i}$ and $s^{r}_{i+1}$,
      respectively, to extract $m$ number of
      objects;
    Compute bounding box around the $m$
      holes in each scan and their centroids
      $P^{m}_{i}$ and $P^{m}_{i+1}$;
    Compute vectors from centroids $P^{m}_{i}$ and
      $P^{m}_{i+1}$ to the centers of $s^{o}_{i}$ and $s^{o}_{i+1}$, i.e.
      $c^{o}_{i}$ and $c^{o}_{i+1}$, respectively;
    Compare the vectors in the successive
      scans to determine $t_x$ and $t_y$;
    Calculate $t_z = d_{i} - d_{i+1}$;
    Transform $s^{o}_{i+1}$ with respect to $s^{o}_{i}$:
      $\hat{s}^{o}_{i+1} = \mathbf{R}.s^{o}_{i+1} + \mathbf{T}$;
end
```

Algorithm 1: 3D Scan Registration.

(Experiment 2), as shown in Figure 6. Scanning was done at an integration time of 200 ms. Experiment 1 contained 35 scans while Experiment 2 contains 357 scans. In both cases, loop closure was ensured to help in the evaluation process while the ground truth was obtained via physical measurements of the different room dimensions.

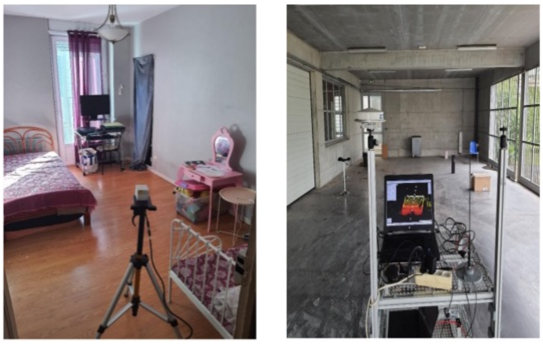

(a)

(b)

Figure 6: (a) and (b) show the experimental setup for Experiment 1 and Experiment 2.

Using these data, the proposed method is compared with a state-of-the-art Global Iterative Closest Point (G-ICP) (Aijazi et al., 2019) and Fast Point Feature Histograms FPFH methods (Rusu and Cousins, 2011).

5.1 Registration Accuracy

The registration results for both experiments are presented in Figure 7. A quantitative analysis is presented in Table 2 for the two experiments and compared with the state-of-the-art methods. ΔE presents the registration error calculated in terms of average absolute difference in dimensions (width and height) of all the walls as compared to the ground truth (similar to Aijazi et al. (2013)).

Table 2: Registration Accuracy for Experiment 1 and Experiment 2.

	Experiment 1 ΔE (m)	Experiment 2 ΔE (m)
Proposed method	0.018	0.043
G-ICP Aijazi et al. (2019)	0.012	0.024
FPFH Rusu and Cousins (2011)	0.017	0.044

The results show that the proposed method is comparable to the other state-of-the-art methods in terms of accuracy. The registration accuracy of the proposed method was better in Experiment 1 and closer to G-ICP as the room size was small and there were less number of scans. In case of Experiment 2, G-ICP outperforms the other methods. This is because, in the G-ICP algorithm, there is a bundle adjustment step at the end to improve the overall scan registration. So the number of scans (or size of acquisition) has less impact on the overall results, whereas in the proposed method, the registration error usually tends to accumulate more with larger number of scans (acquisition size) as seen in the results.

5.2 Processing Time

The proposed method along with the other state-of-the-art methods were run on the same laptop (processor Intel Core i9-10885H, CPU @ 2.40 GHz, memory 32 GB) under Windows 10 operating system. The results of the registration time (in seconds) are presented in Table 3.

From the results, it can be seen that there is not a significant difference in the processing time, especially in case of Experiment 1, at this lower scan resolution (number of points per scan).

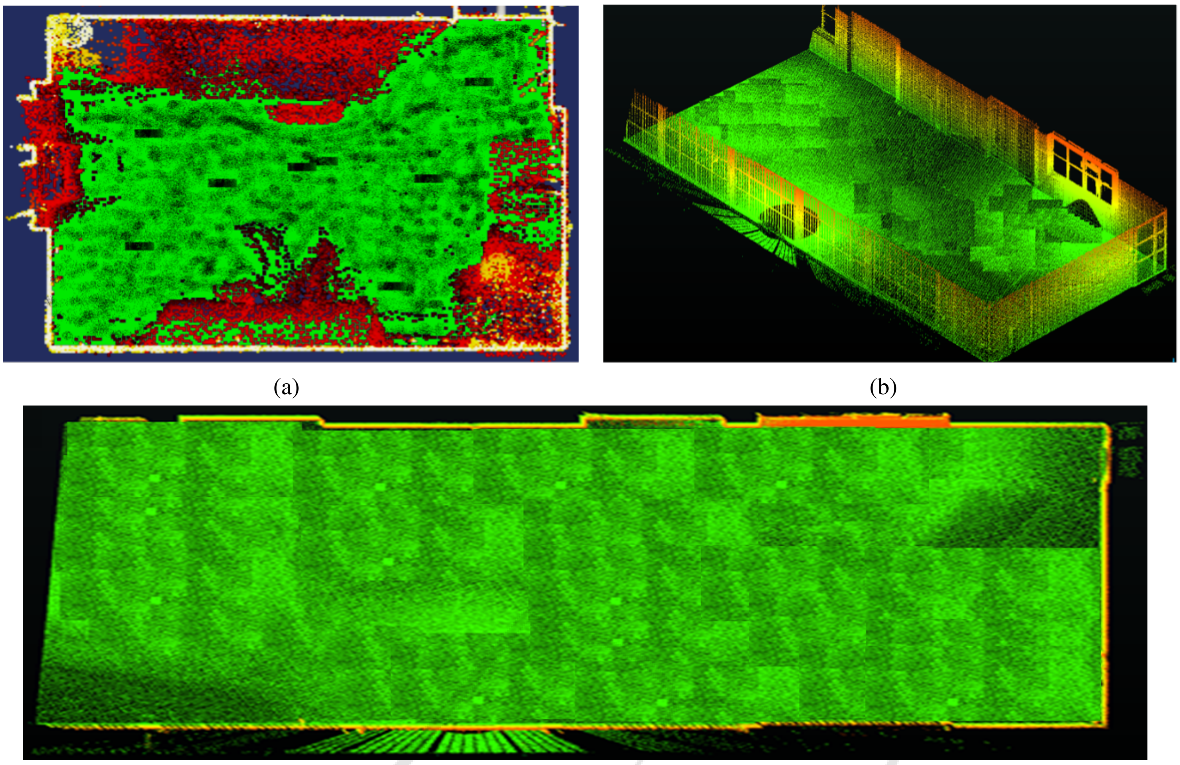

(a)

(b)

(c)

Figure 7: (a), (b) and (c) show the registration results for Experiment 1 and Experiment 2 employing the proposed method.

Table 3: Processing time.

	Experiment 1 (s)	Experiment 2 (s)
Proposed method	90	900
G-ICP Aijazi et al. (2019)	100	1700
FPFH Rusu and Cousins (2011)	95	1295

As the results presented in Table 3 were inconclusive, the Experiment 1 was repeated at different scan resolutions by varying the data integration time, i.e. from 200 ms (low resolution) to 500 ms (high resolution). The results are presented in Table 4.

Table 4: Processing time for different scan resolutions.

	200 ms	300 ms	400 ms	500 ms
Proposed method	90 s	155 s	205 s	289 s
G-ICP Aijazi et al. (2019)	100 s	250 s	480 s	875 s
FPFH Rusu and Cousins (2011)	95 s	197 s	352 s	615 s

The results demonstrate the strength of the proposed method in terms of computational time as the number of points per scan increases. For methods like G-ICP, the processing time increases manifold with the increase of number of points as the number of correspondences between points increases. However, the proposed method remains relatively unchanged. This makes it more suitable for real time applications.

6 CONCLUSION

In this paper, a novel 3D registration method is presented that exploits the unique scanning pattern of the sensor to register successive 3D scans. The method was evaluated on real data and compared with other state-of-the-art methods that show the prowess of the proposed method. The results show that the method is comparable with other methods in terms of accuracy but surpasses them in performance in terms of processing speed. In the proposed method, slight drift in error is observed in case of larger distance and number of scans. However, in terms of processing time, it is shown to be invariant to increase in number of 3D points per scan. For future, we would like to improve the accuracy of the method by incorporating some constraints like loop closure, whereas it would also be considered to use an ICP method to further improve or fine register the resulting point cloud.

ACKNOWLEDGEMENTS

This work is supported by the International Research Center "Innovation Transportation and Production Systems" of the I-SITE CAP 20−25. Financial support was also received from the Auvergne-Rhône-Alpes region through the ACCROBOT project (AC-Costage haute précision ROBOTisé − Chantier Transitique du laboratoire FACTOLAB) as part of the Pack Ambition Recherche 2020.

REFERENCES

Aijazi, A. K., Checchin, P., and Trassoudaine, L. (2013). Automatic removal of imperfections and change detection for accurate 3d urban cartography by classification and incremental updating. *Remote Sensing*, 5(8):3701–3728.

Aijazi, A. K., Malaterre, L., Trassoudaine, L., Chateau, T., and Checchin, P. (2019). Automatic Detection and Modeling of Underground Pipes Using a Portable 3D LiDAR System. *Sensors*, 19(24).

Besl, P. and McKay, N. (1992). A Method for Registration of 3-D Shapes. *IEEE Trans. on PAMI*, 14(2):239–256.

Brazeal, R. G., Wilkinson, B. E., and Hochmair, H. H. (2021). A Rigorous Observation Model for the Risley Prism-Based Livox Mid-40 Lidar Sensor. *Sensors*, 21(14).

Choy, C., Dong, W., and Koltun, V. (2020). Deep Global Registration. In *Proceedings of the IEEE Computer Society Conference on Computer Vision and Pattern Recognition*, pages 2511–2520.

He, Y., Ma, L., Jiang, Z., Tang, Y., and Xing, G. (2021). VI-Eye: Semantic-Based 3D Point Cloud Registration for Infrastructure-Assisted Autonomous Driving. In *Proceedings of the 27th Annual International Conference on Mobile Computing and Networking*, MobiCom '21, page 573–586, New York, NY, USA.

Klasing, K., Althoff, D., Wollherr, D., and Buss, M. (2009). Comparison of surface normal estimation methods for range sensing applications. In *2009 IEEE International Conference on Robotics and Automation*, pages 3206–3211.

Li, H., Zhao, H., Ye, B., and Zhang, Y. (2023). 3D semantic map construction based on point cloud and image fusion. *IET Cyber-Systems and Robotics*, 5(1):e12078.

Pais, G. D., Ramalingam, S., Govindu, V. M., Nascimento, J. C., Chellappa, R., and Miraldo, P. (2019). 3DRegNet: A Deep Neural Network for 3D Point Registration. In *Proceedings of the IEEE Computer Society Conference on Computer Vision and Pattern Recognition*, pages 7191–7201.

Rusu, R. B., Blodow, N., and Beetz, M. (2009). Fast Point Feature Histograms (FPFH) for 3D registration. In *IEEE International Conference on Robotics and Automation*, pages 3212–3217.

Rusu, R. B. and Cousins, S. (2011). 3D is here: Point Cloud Library (PCL). In *IEEE International Conference on Robotics and Automation (ICRA)*, pages 1 – 4.

Segal, A., Haehnel, D., and Thrun, S. (2009). Generalized-ICP. In *Robotics: Science and Systems*, volume 5, pages 168–176.

Serafin, J. and Grisetti, G. (2015). NICP: Dense normal based point cloud registration. In *IEEE International Conference on Intelligent Robots and Systems*, volume 2015-Decem, pages 742–749.

Tazir, M. L., Gokhool, T., Checchin, P., Malaterre, L., and Trassoudaine, L. (2018). CICP: Cluster Iterative Closest Point for sparse-dense point cloud registration. *Robotics Auton. Syst.*, 108:66–86.

Wang, Y., Bu, S., Chen, L., Dong, Y., Li, K., Cao, X., and Li, K. (2023). HybridFusion: LiDAR and Vision Cross-Source Point Cloud Fusion.

Wang, Z., Wang, X., Fang, B., Yu, K., and Ma, J. (2021). Vehicle detection based on point cloud intensity and distance clustering. *Journal of Physics: Conference Series*, 1748(4):042053.

Xie, Z., Liang, P., Tao, J., Zeng, L., Zhao, Z., Cheng, X., Zhang, J., and Zhang, C. (2022). An Improved Supervoxel Clustering Algorithm of 3D Point Clouds for the Localization of Industrial Robots. *Electronics*, 11(10).

Xue, G., Wei, J., Li, R., and Cheng, J. (2022). LeGO-LOAM-SC: An Improved Simultaneous Localization and Mapping Method Fusing LeGO-LOAM and Scan Context for Underground Coalmine. *Sensors*, 22(2).

Zou, Z., Lang, H., Lou, Y., and Lu, J. (2023). Plane-based global registration for pavement 3D reconstruction using hybrid solid-state LiDAR point cloud. *Automation in Construction*, 152:104907.